Materials Science and Engineering B 325 (2026) 119160

Contents lists available at ScienceDirect

Materials Science & Engineering B

journal homepage: www.elsevier.com/locate/mseb

Inkjet printing of hard magnetic iron-platinum thin films

Roberto Bernasconi [a,*], Francesca Casoli [b], Luca Magagnin [a]

[a] Dipartimento di Chimica, Materiali e Ingegneria Chimica "Giulio Natta", Politecnico di Milano, Via Mancinelli 7, 20131 Milano, Italy
[b] CNR-IMEM, Parco Area delle Scienze 37/A, 43124 Parma, Italy

ARTICLE INFO

Keywords:
Inkjet printing
Nanoparticles
Thin films
FePt
Hard magnetic

ABSTRACT

FePt alloys are known for their exceptional hard magnetic properties, which translate into high coercivity, saturation magnetization and energy product. Their capability to efficiently retain permanent magnetization makes them attractive for applications like data storage, sensors, energy harvesters, microactuators and biomedical microrobotics. The present study investigates the deposition of hard magnetic FePt thin layers via inkjet printing (IJP), providing the first demonstration of FePt thin films deposition using this versatile and scalable technique. FePt nanoparticles (NPs) are synthesized using a facile water-based reduction method and subsequently dispersed in a green organic solvent to formulate printable inks. The inkjet printing process is optimized to achieve uniform layers with controlled thickness, which are annealed in a reducing atmosphere at various temperatures to induce the formation of the chemically ordered $L1_0$ phase. A comprehensive morphological, structural, and magnetic characterization confirms the formation of uniform and adherent layers with significant coercivity and magnetization, particularly after annealing at 750 °C. Under these conditions, a coercivity up to 794 mT and a remanence up to 36 A m^2 kg^{-1} can be obtained. The results obtained indicate that inkjet printing is a viable and scalable technique for producing high-performance FePt magnetic layers, with potential applications in many industrial sectors.

1. Introduction

The nearly equiatomic alloy formed by iron and platinum is well-known for its attractive hard magnetic properties [1]. Indeed, iron concentrations between 35 and 55 % at. result in the formation of the $L1_0$ superstructure, where the cubic symmetry is broken by the stacking of alternate planes of Fe and Pt atoms [2]. As a consequence of the high anisotropy typical of this configuration, FePt alloys in the $L1_0$ phase present excellent hard magnetic properties, with high values of coercivity, saturation magnetization and energy product. Thanks to these exceptional features, FePt finds potential applicability in a wide variety of fields [3]. In particular, thin films of this alloy can be used to manufacture high-density recording media [4], powerless sensors, microactuators [5] and magnetic energy harvesting systems. Unlike most of the alternative hard magnetic materials [6], FePt is biocompatible and, thanks to this peculiarity, it can be used in biomedical applications that require the use of magnetic fields, like the realization of untethered microrobots [7,8].

From the manufacturing point of view, FePt can be deposited as thin films employing techniques like sputtering [9,10], pulsed laser deposition [11] or electrodeposition [12–15]. In alternative to these two methodologies, which require the use of masks in order to get patterned layers, a possible way to deposit FePt layers can be inkjet printing (IJP) [16–18]. This technique, based on the jetting of droplets of a fluid ink from a nozzle, potentially allows depositing patterned FePt layers having controlled thickness in a scalable and costless way. In addition, inkjet printing allows controlling the magnetic anisotropy of the printed layers, introducing the possibility of magnetic axis programming [19,20]. Obviously, IJP requires the use of fluid inks, having well-defined and controlled rheological properties [21]. Consequently, solid magnetic materials can only be printed in the form of a sol-gel precursor or as a dispersion of nanoparticles (NPs) in a solvent. The first method offers significant challenges when applied to the realization of continuous layers, which are difficult to obtain in a crack free and adherent form. NPs, on the contrary, are easy to synthesize and disperse. Many examples of IJP of magnetic materials, employing both sol-gels and NPs, are available in literature. Most of these materials are soft magnetic ferrites like Ni—Zn [22,23], Mn—Zn [24] or Bi [25] ferrites. More recently, however, also the IJP of hard magnetic ferrites has been demonstrated [26].

* Corresponding author.
E-mail address: roberto.bernasconi@polimi.it (R. Bernasconi).

https://doi.org/10.1016/j.mseb.2025.119160
Received 2 October 2025; Received in revised form 30 November 2025; Accepted 23 December 2025
Available online 29 December 2025

Table 1
Chemicals employed for the preparation of the three types of NPs used. The table also reports the expected Pt/(Pt + Fe) ratio.

	K_2PtCl_6 (g)	$FeCl_3$ (g)	Triton X-102 (g)	Expected Pt/(Pt + Fe)
Pt-poor	0.4	0.259	0.6	0.34
Equimolar	0.4	0.134	0.6	0.50
Pt-rich	0.4	0.096	0.6	0.58

For what concerns FePt, the most practical way to get IJP printable inks is the use of NPs. Typical reaction routes for FePt NPs production are based on solvothermal/ hydrothermal reactions [27–29], on the use of alternate reduction [30], gas phase aggregation [31], ball milling [32] or photoreduction [33]. The use of the sol-gel approach, on the contrary, is typically not viable to get continuous layers of FePt, but it can be successfully applied to synthesize NPs having highly controlled dimensions and magnetic properties [34]. FePt NPs can be easily stabilized and dispersed in both aqueous [35] and non-aqueous environment [36,37], obtaining thus inks potentially suitable for IJP. Nevertheless, to the best of our knowledge nobody ever tried to print these dispersions and the IJP of continuous FePt layers is currently still unexplored.

In this context, the present work aims at depositing for the first time thin layers of hard magnetic FePt alloy by means of IJP. The starting point of the work is the straightforward synthesis of narrowly dispersed FePt NPs through a simple reaction strategy based on the use of inorganic precursors. Providing a simple and reproducible synthesis procedure, which does not rely on the use of metalorganic precursors or high temperatures, is important for the cost-effective production of FePt nanoparticles. FePt NPs, in addition, often require organic coatings to ensure stability in solution. The NPs obtained in the present work, on the contrary, are directly dispersed in a green solvent without the use of any additional surfactant and subsequently inkjet printed. In particular, Cyrene is selected as solvent due to its high boiling point, its good biodegradability [38] and its ability to yield stable dispersions of NPs [39]. The printability of the resulting inks is evaluated and the patterning potential of the IJP process is investigated. Finally, the FePt layers are annealed in a reducing atmosphere to promote the formation of the highly ordered $L1_0$ phase and subsequently characterized from the morphological, microstructural and magnetic point of view. If compared to other magnetic materials commonly printed via inkjet, such as ferrites and magnetite, the printing process of FePt presents some peculiarities that justify its investigation. In particular, the IJP of surfactant-free dispersions of FePt has never been attempted and the process can be challenging to optimize from the printability point of view. FePt nanoparticles are characterized by a high density, which can lead to rapid sedimentation in the ink, causing long-term stability issues and printhead clogging. Finally, the inkjet printing and sintering of FePt nanoparticles requires precise control of the crystallographic orientation to achieve the desired hard magnetic properties and this can be difficult to achieve using a printing process. For what concerns possible applications of IJP FePt layers, they can be identified considering the strengths of the technique employed. The high resolution patterning typical of IJP, in particular, suggests the realization of powerless magnetic sensors and energy harvesting systems as the most realistic potential applicative fields. In these fields, the superior versatility of IJP for printing micromagnets of the desired shape represents a further advantage compared to lithographic techniques, even compared to costless solutions like molding [40].

2. Experimental methods

2.1. Chemicals employed

K_2PtCl_6 (CAS number 16921–30-5, ≥ 98 % purity), $FeCl_3$ (CAS number 7705-08-0, ≥ 98 % purity), Triton X-102 (CAS number 9036-19-5), hydrazine monohydrate (65 % wt. in water solution, CAS number 7803-57-8, 98 % purity) and Cyrene (dihydrolevoglucosenone, CAS number 53716–82-8, ≥ 98.5 % purity) were purchased from Sigma Aldrich and used as received.

2.2. FePt NPs synthesis

Three types of NPs were synthesized: Pt-poor, equimolar and Pt-rich. Table 1 reports the amount of chemicals used for each synthesis.

For each type of NPs, the following steps were followed:

1. Preparation of solution A: K_2PtCl_6 + $FeCl_3$ + Triton X-102 + water to reach 200 mL.
2. Preparation of solution B: 10 mL of hydrazine monohydrate solution +15 mL of water.
3. Heating of solution A to 65 °C.
4. Dropwise addition of solution B in solution A (at 700 rpm).
5. Reaction for 30 min and cooling to room temperature.
6. Centrifugation and washing with ethanol.

To avoid oxidation and aggregation, at the end of the washing procedure the NPs were dried in vacuum.

2.3. FePt inks preparation

To prepare the inks, 2 % wt. of FePt NPs were dispersed in Cyrene. The resulting dispersion was probe sonicated in a TU-900Y setup (Toption Group Ltd) for 10 min at 70 % of the maximum power. The diameter of the probe was 6 mm, the on time was 2 s and the off time was 2 s. The inks showed no sign of precipitation for at least 1 week.

2.4. Inkjet printing

FePt was inkjet printed with a Dimatix DMP (Fujifilm) setup, equipped with standard 10 pL cartridges. The temperature of the plate was set at 60 °C, while the temperature of the printhead was set at 45 °C. A single pulse waveform was used, with the potential varying between 26 and 38 V. The jetting frequency was set at 10 kHz and the drop spacing (DS) employed was varied between 20 and 140 μm. Silicon wafer chips were used as substrates for the printing tests. The chips were sonicated in water for 5 min and then in acetone for 5 min. After rinsing, they were carefully dried and treated with atmospheric plasma for 30 s in order to enhance wettability. 5 × 5 mm squares were printed on the silicon substrates and between 2 and 10 layers were employed in order to determine the growth rate of the films with respect to the number of printing cycles. An interlayer delay equal to 300 s was employed in order to allow solvent evaporation. The samples were cut to observe the cross section and the thickness of the deposited material was determined via SEM. For what concerns the samples used for the morphological and magnetic characterizations, 5 × 5 mm squares with 10 layers of FePt were printed using a drop spacing of 20 μm, also in this case with an interlayer delay equal to 300 s.

2.5. Annealing of the FePt layers

The inkjet printed layers were annealed in a Carbolite tubular oven. An atmosphere containing 5 % H_2 in argon was employed. The samples were annealed at 650 °C for 1 h or at 750 °C for 2 h.

2.6. Characterization techniques

The viscosity of the inks was measured using a DSR200 rheometer (Rheometrics), equipped with planar plates. The surface tension of the inks was extrapolated considering the contact angle value measured placing a droplet of the ink itself on a surface with a known surface energy (specifically, sputtered gold). Such contact angle was measured using a micro camera and the Drop Shape software. The density of the ink was simply evaluated by measuring the weight of 1 mL of ink with a

Table 2
Expected vs. experimental Pt/(Pt + Fe) ratio and O content for the three types of NPs.

	Expected Pt/(Pt + Fe)	Experimental Pt/(Pt + Fe)	Yield [%]	O content [% at.]
Pt-poor	0.34	0.356	83.4	20.2 ± 0.99
Equimolar	0.50	0.505	81.2	19.6 ± 0.64
Pt-rich	0.58	0.549	82.7	19.3 ± 0.66

precision balance. SEM was carried out using a EVO 50 EP setup (Zeiss). Such instrument was equipped with an energy dispersive spectroscopy (EDS) unit model Inca Energy 200 (Oxford Instruments). TEM was carried out employing a CM200 setup (Philips). The size distribution of the NPs was evaluated using the open-source software ImageJ. A large number (> 500) of NPs was randomly selected and the maximum diameter of each particle was directly measured using the software. The X-ray diffraction (XRD) characterization of the FePt layers was carried out using a PW1830 diffractometer (Philips), with a $Cu_{K\alpha}$ source and in Bragg-Brentano configuration. The height profile of the layers was acquired by means of a UBM Microfocus (UBM) laser profilometer. A Dimension 3100 Scanning Probe Microscope equipped with a Nanoscope Veeco controller was employed to study the surface topography (AFM) and stray field magnetic contrast (MFM) of the layers. The two types of contrast were detected operating the instrument in tapping mode, using MESP-V2 tips (Bruker). The room temperature magnetic properties of the samples were investigated by Alternating Gradient Force Magnetometry (AGFM). Hysteresis curves were measured by AGFM by applying a maximum field of 2 T, both parallel and perpendicular to the substrate surface. A Quantum Design PPMS Dynacool system equipped with a Vibrating Sample Magnetometer (VSM) was employed to measure the hysteresis curves of the samples annealed at 750 °C in the field range ± 9 T.

3. Results and discussion

3.1. NPs synthesis and characterization

As a first step of the experimentation, the FePt NPs were synthesized by direct reduction of the metallic precursors in aqueous environment. Three nominal compositions were selected in order to explore the magnetic properties of alloys containing different concentrations of the two metals. In addition to the equiatomic one, two additional

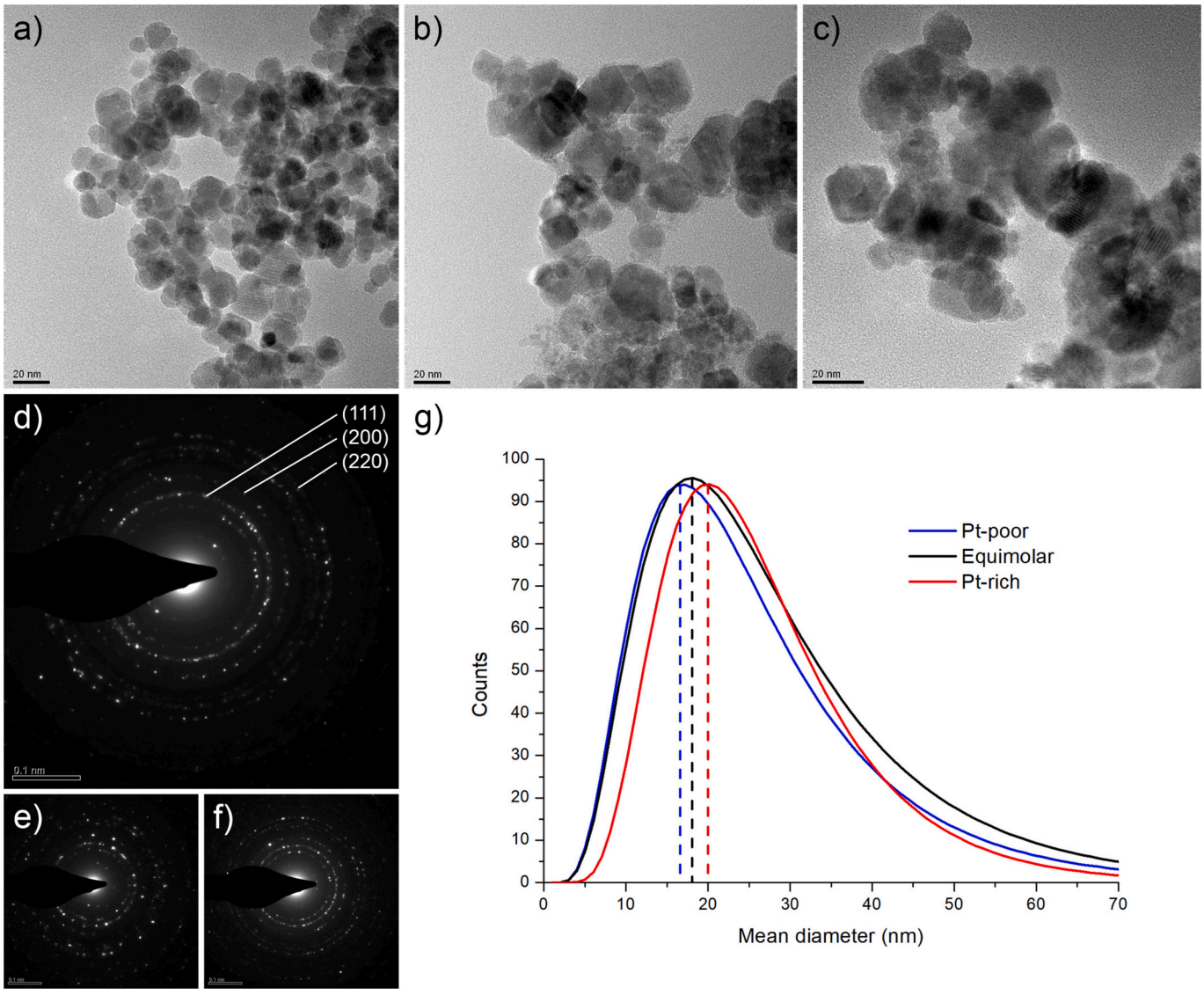

Fig. 1. TEM characterization of the (a) Pt-poor, (b) equimolar and (c) Pt-rich NPs; SAED patterns for the (d) equimolar, (e) Pt-poor and (f) Pt-rich NPs; (g) interpolated size distributions for the three types of FePt NPs.

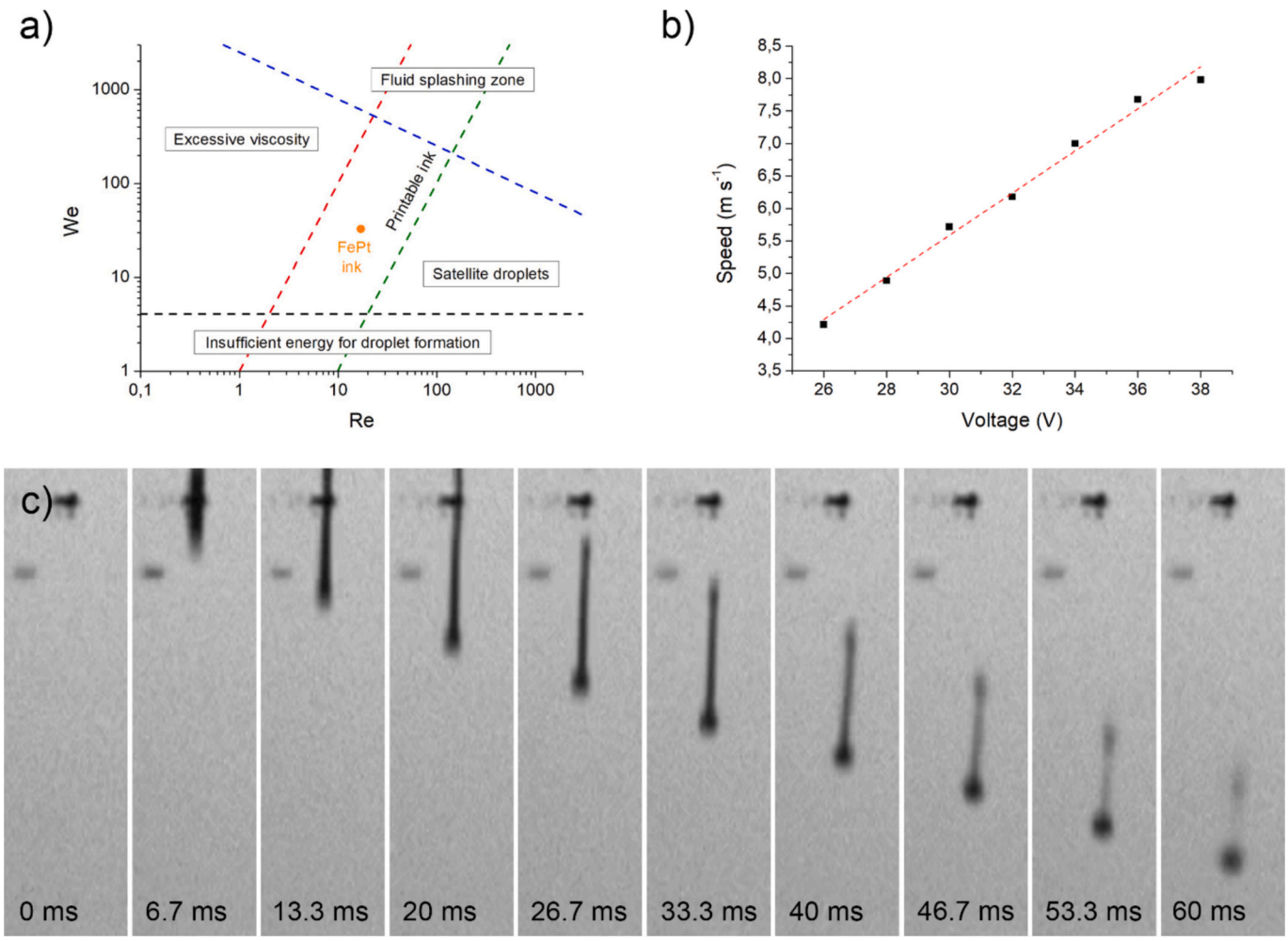

Fig. 2. (a) printability evaluation for the equimolar FePt ink, evaluated at 7 m s^{-1}; (b) speed vs. voltage relationship for the jetting of the equimolar FePt ink; (c) droplet formation stages for the equimolar FePt ink, jetted at 34 V.

compositions located at the diametrically opposite margins of the $L1_0$ phase stability region were selected: 34 % at. Pt and 58 % at. Pt. These compositions are located, on the FePt phase diagram, in close proximity of the stability zone boundaries for Fe_3Pt and $FePt_3$ intermetallics, respectively [41]. The yield of the synthesis process, regardless of the type of NPs produced, always exceeded 80 % (Table 2).

The as prepared NPs were characterized from the morphological and compositional point of view. The first characterization carried out was EDS, in order to determine their elemental composition (Fig. S1). Table 2 reports the results obtained for what concerns the experimental Pt/(Pt + Fe) atomic ratio and the oxygen present in the NPs. It appears evident that the Pt concentration obtained experimentally slightly diverged from the expected one. The deviations observed, however, were relatively limited and corresponded to 4.7 % in the case of the Pt-poor NPs, 1 % for the equiatomic NPs and 5.3 % for what concerns the Pt-rich NPs. As a consequence, the NPs obtained were still representative of the compositional spectrum of the $L1_0$ phase. The EDS analysis carried out on the as-prepared NPS also evidenced the presence of a relevant amount of oxygen, which is typically incorporated in the NPs as an impurity during the reduction process.

The as-synthesized NPs were characterized at the TEM (Fig. 1). Figures from 1a to 1c, in particular, depict the morphology of the Pt-poor, equimolar and Pt-rich NPs, respectively. Some additional TEM images have been included in the Supplementary Material (Figures from S2 to S4). All the three types of NPs show a tendency to agglomerate when the solvent is removed. The shapes of the NPs, regardless of the composition, look prevalently equiaxial and rounded, even though a minority of polyhedral particles can be observed (especially in Fig. 1a and b).

The SAED patterns (Figures from 1d to 1f) evidenced the presence of the typical diffraction features associated to the presence of a disordered fcc FePt phase. In particular, the (111), (200) and (220) rings are quite evident and are present, without any significant variation, in all the SAED patterns acquired. Besides the features associated with FePt, some relatively strong additional rings can be observed in all the samples. These are reasonably produced by secondary phases, like oxides and hydroxides, generated during the reduction process in aqueous environment. Their presence, indeed supported by the relevant oxygen content detected in the NPs, is probably connected to the use of hydrazine, which increases the pH during the reduction of K_2PtCl_6 and $FeCl_3$ allowing the possible formation of iron oxides [42].

The size distribution of the FePt nanoparticles was evaluated analyzing the TEM images acquired. Figures from S5 to S7 report the raw data obtained, while Fig. 1g shows the comparison between the fittings operated on the three sets of raw data. It appears evident that there is a difference in the mean size of the particles, which changes from 20.19 nm for the Pt-rich NPs to 18.14 nm for the equimolar NPs and 16.73 nm in the case of the Pt-poor NPs.

3.2. *Inkjet printability evaluation*

When dispersed in Cyrene, all the FePt NPs yielded dispersions stable

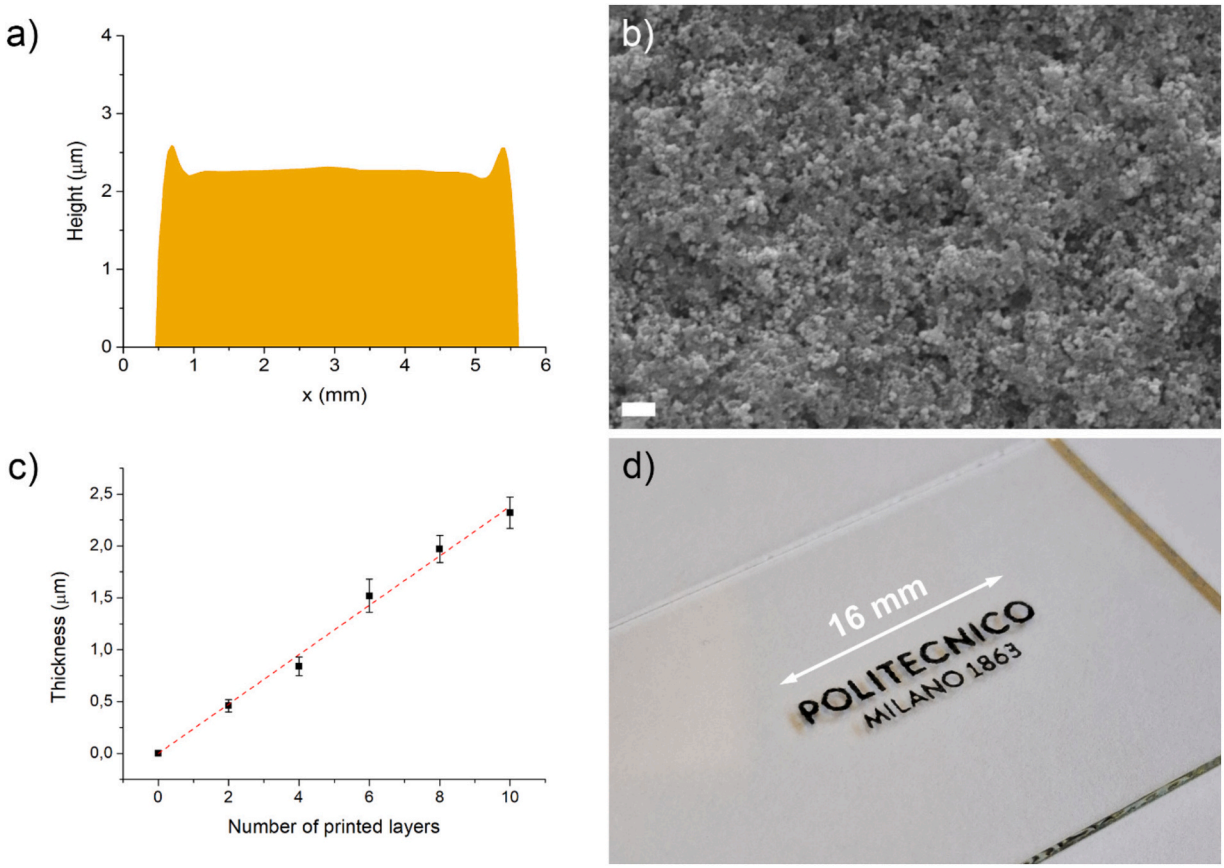

Fig. 3. (a) height profile of an equimolar FePt layer printed on Si with 10 layers; (b) SEM image of an as-printed layer of equimolar FePt NPs (scale bar 1 μm); (c) thickness vs. number of layers relationship for the equimolar FePt ink; (d) Politecnico di Milano logo printed on glass.

enough to be efficiently jetted in a Dimatix 10 pL inkjet cartridge. Initially, the theoretical printability of the inks was evaluated by calculating the Ohnesorge number (Eq. 1), which corresponds to the ratio between the square root of the Weber number (*We*) and the Reynolds number (*Re*).

$$Oh = \frac{\sqrt{We}}{Re} = \frac{\mu}{\sqrt{\rho\gamma D}} \quad (1)$$

Oh does not depend on the speed of the jetted droplet and it correlates viscous, inertial and surface tension forces. Indeed, it contains μ (dynamic viscosity), ρ (density), γ (surface tension) and D (characteristic length). In the case of inkjet printing, D corresponds to the dimension of the nozzle (19 μm). The density of the ink, its surface tension and its viscosity were all evaluated experimentally and they resulted equal to 1.53 g cm^{-3}, 45 mN m^{-1} and 12.3 cPs, respectively. Consequently, the Ohnesorge number resulted equal to 0.34. This value, falling in the 0.1–1 range, is indicative of a fully jettable ink [43]. No significant differences were observed between the three inks.

Suitable values of *Oh* constitute a first indication of printability. However, following a more rigorous approach, the speed of the droplet must be considered as well. This can be done by separately evaluating *We* and *Re* at a fixed speed of the droplets and comparing the resulting values with reference printability charts. Fig. 2a reports the position of the FePt ink developed in the present work on the printability chart described by Derby et al. [44]. The evaluation was done considering a speed of the droplets of 7 m s^{-1}. Such speed is the minimum one recommended by the manufacturer of the Dimatix printer in order to get optimal precision. Under these conditions, the ink falls exactly in the middle of the printability region.

The speed of the droplets was efficiently controlled modifying the actuation potential of the piezoelectric element embedded in the printhead, as reported in Fig. 2b. The dependence of the droplet speed from the voltage applied to the piezoelectric actuator is basically linear and the optimal jetting speed of 7 m s^{-1} is achieved at 34 V. The behavior of the three inks was found to be similar, regardless of the composition of the NPs employed for their formulation.

The theoretical jettability of the FePt ink was confirmed experimentally by observing the jetting process with the stroboscopic camera embedded into the Dimatix machine (Fig. 2c). The composite image shows the stages of droplet formation at different times (with an actuation potential equal to 34 V). Initially, the droplet is ejected from the nozzle in an elongated form, characterized by the presence of the so-called tail. When it fully detaches from the nozzle, however, the tail tends to be reabsorbed and its length progressively decreases over time. At the end, after a time longer than 60 ms, a fully spherical droplet is obtained. The droplets were found to totally reabsorb their tails at any potential, but the time required by the process was found to increase considerably at the highest jetting potentials (from 36 V up to the maximum potential that the printer can apply, 40 V).

3.3. FePt printing tests

Following the preliminary printability assessment, FePt continuous layers were deposited on silicon. The silicon substrate was subjected to plasma treatment in all the printing tests, in order to increase its surface energy and favor ink spreading. In absence of any pretreatment, indeed, the FePt ink tends to coalesce forming islands of material with exposed substrate areas in between. On plasma treated silicon, on the contrary, the ink distributes uniformly.

In order to evaluate the minimum achievable feature size, which is indicative of the precision of the printing process, single lines of ink were

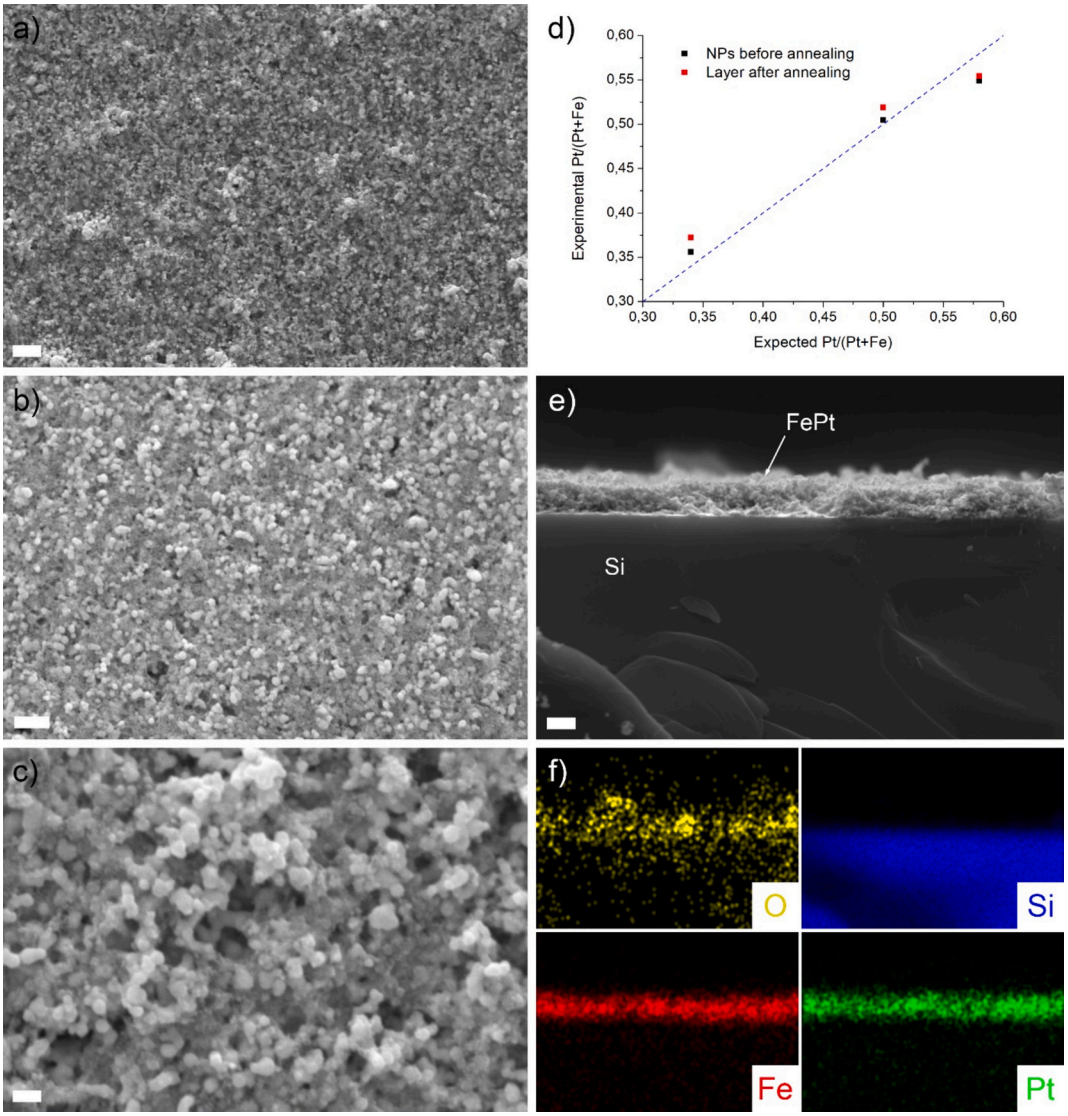

Fig. 4. SEM images of the top surface of (a) equimolar (scale bar 2 μm), (b) Pt-poor (scale bar 1 μm) and (c) Pt-rich (scale bar 400 nm) FePt layers annealed at 750 °C for 2 h; (d) layers composition before and after annealing at 750 °C for 2 h; (e) SEM image of the cross-section of an equimolar FePt layer annealed at 750 °C for 2 h (scale bar 2 μm); (f) EDS elemental mapping of the cross-section of an equimolar FePt layer annealed at 750 °C for 2 h.

inkjet printed and their width was evaluated as a function of the drop spacing employed. The distance between two consecutive droplets influences the amount of material deposited and consequently the spreading of the material itself on the silicon surface. The width was directly measured at the optical microscope and the results obtained are reported in fig. S8. When the drop space is excessive, the droplets cannot merge and the width of the line corresponds to the diameter of the droplets (roughly 50 μm). As the drop spacing decreases, in turn, droplets start to merge and form a continuous line, whose width depends on the drop spacing itself. In the case of continuous lines, the minimum obtainable feature size is comprised between 70 and 85 μm (at drop spacings between 20 and 50 μm).

Following this first printing test, continuous squares of material were printed on silicon. The drop spacing used was selected prioritizing the growth rate of the layer over precision. The use of 20 μm as drop spacing, indeed, allowed getting relatively thick layers of FePt printing a reduced number of layers. For applications where a high precision is required, it may be convenient to increase the drop spacing in order to improve the minimum achievable feature size. In this case, however, a larger number of printing cycles is required to get thick layers. The printing plate was heated in order to limit the impact of the coffee ring effect [45]. This phenomenon is the main responsible for uneven film formation in inkjet printed layers and it is normally detected as an increased thickness in correspondence of the edges of the printed layer. Different strategies can be implemented to reduce the formation of coffee rings [46], but the most commonly used is substrate heating.

Fig. 3a shows the height profile of a FePt layer printed with 10 layers. Thanks to the heating applied to the plate of the printer, a reduced coffee ring effect was observed in the case of FePt jetting on the silicon substrates employed in the present work. For what concerns the morphology of the printed material, the SEM characterization evidenced a relatively uniform appearance, with some evident degree of porosity (Fig. 3b).

The dependence of the thickness of the resulting layers of FePt from the number of printing cycles was evaluated by looking at the cross section in the middle of the printed area. The graph obtained shows a linear growth tendency, as evidenced by Fig. 3c. The most interesting characteristic of IJP is its capability of depositing the material of interest in the form of complex shapes. To demonstrate this capability in the case of the FePt ink developed in the present work, the Politecnico di Milano logo was printed on glass (with 5 layers of FePt equimolar ink). The resulting pattern contains features having dimensions down to 140 μm

Table 3
Comparison between the composition measured by EDS before and after the annealing process. Oxygen content is reported for the annealed layers only.

	Annealing temperature [°C]	Annealing time [h]	As printed Pt/(Pt + Fe)	Annealed Pt/(Pt + Fe)	O content [% at.]
Pt-poor	750	2	0.356	0.372	3.21 ± 0.13
Equimolar	650	1	0.505	0.509	6.28 ± 0.54
Equimolar	750	2	0.505	0.519	3.45 ± 0.11
Pt-rich	750	2	0.549	0.554	3.11 ± 0.24

(fig. 3d).

3.4. Morphological and compositional characterization

Following the printing step, the layers were annealed in a reducing atmosphere in order to decrease their oxygen content, promote partial sintering and trigger $L1_0$ phase formation. The SEM images acquired at the end of the sintering process demonstrate that the morphology of the coatings significantly changed upon exposure to 750 °C for 2 h (Figures from 4a to 4c and from S9 to S11). The final appearance of the samples was found to be similar regardless of the composition of the FePt NPs employed and it was characterized by the absence of cracks and by the presence of some residual porosity. Considering similar inkjet printed and annealed layers, composed of nanoparticles of comparable size, the typical value for residual porosity can be around 10 %. This is the case, for example, of annealed silver nanoparticles [47]. The occurrence of a partial sintering is especially evident in Fig. 4c, where necking and partial particles fusion can be seen.

For what concerns the composition of the particles at the end of the annealing step, the numerical data obtained from the EDS analysis are reported in Table 3 and visually represented in Fig. 4d.

The first important observation that can be extrapolated from Fig. 4d and Table 3 regards the composition before and after annealing. In general, the Fe content of the layers was found to slightly decrease upon exposure to high temperatures. This effect, already observed by Yuan et al. [48], is probably correlated to the presence of iron oxides in correspondence of the surface, which leaves Fe bleached from the bulk of the NPs. This effect, in connection with the high oxygen content and the presence of secondary phases observed via TEM, suggests that iron oxide is present in correspondence of the surface of the as-printed NPs. Following annealing in the reducing atmosphere, oxygen content was found to strongly decrease (Table 3). In particular, annealed samples contained very low amounts of oxygen, suggesting almost total reduction or removal of any iron oxide present in the layers.

The deposited and annealed samples were broken in a controlled way and the resulting cross-section was observed at the SEM (Fig. 4e). All the images obtained, regardless of the type of nanoparticles, clearly

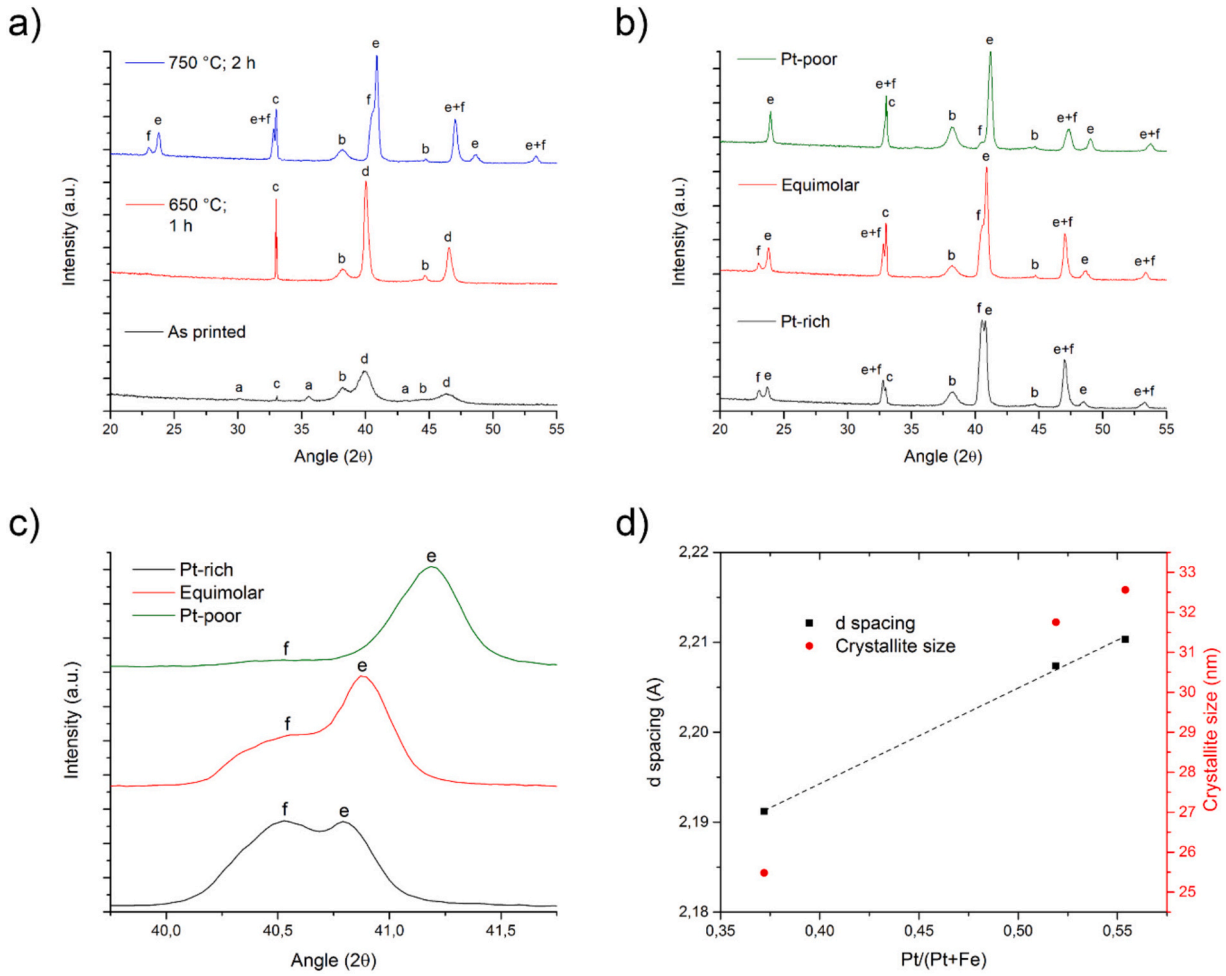

Fig. 5. (a) phase composition of the inkjet printed equimolar FePt layer as a function of annealing conditions; (b and c) phase composition of the inkjet printed FePt layers after annealing at 750 °C as a function of alloy composition; (d) d spacing and crystallite size as a function of alloy composition; peaks identification: a = Fe_2O_3, b = Au, c = Si, d = disordered fcc FePt phase, e = $L1_0$ FePt phase, f = $L1_2$ $FePt_3$ phase.

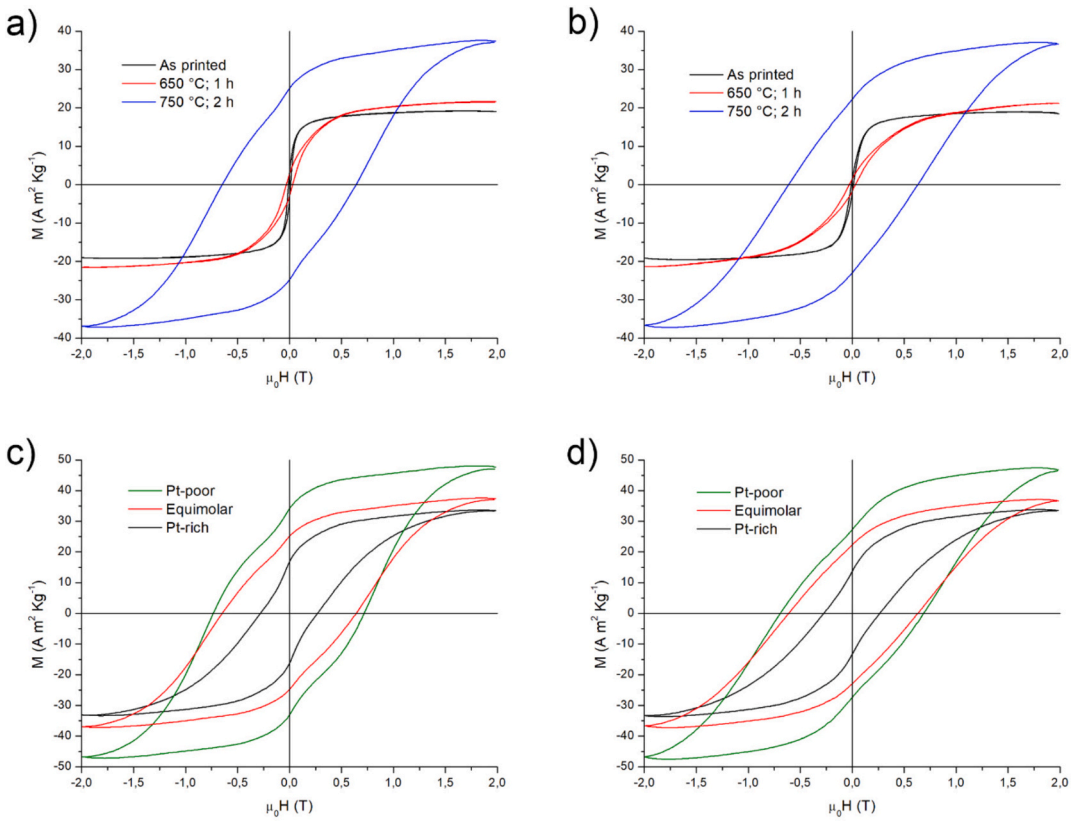

Fig. 6. (a) AGFM in-plane results for the equimolar FePt alloy as a function of annealing temperature; (b) AGFM out-of-plane results for the equimolar FePt alloy as a function of annealing temperature; (c) AGFM in-plane results for alloys annealed at 750 °C as a function of their composition; (d) AGFM out-of-plane results for alloys annealed at 750 °C as a function of their composition.

evidence the presence of adherent and continuous FePt layers. Such layers are characterized by the presence of a residual porosity, in conformity with the SEM images acquired on the top of the samples, and by a mean thickness equal to 2.32 ± 0.15 μm. The EDS mapping performed on the section (Fig. 4f) confirmed the presence of Pt and Fe in correspondence of the FePt layer and evidenced the presence of some residual oxygen inside the layer itself.

3.5. Phase characterization

Fig. 5a reports the phase variations, determined via XRD, observed during the annealing of an inkjet printed equimolar FePt alloy. The silicon signal resulted from the substrate, while the gold signal resulted from the gold layer deposited on the samples for SEM observation. For what concerns FePt, the as printed layer mainly contained a disordered fcc FePt phase [49]. Its presence can be inferred considering the two peaks at 40.1° and 46.4°, which are respectively correlated to the (111) and (200) orientations of the fcc phase (JCPDS card n° 29–0717). In addition to the alloy, the layer also apparently contained an iron-based secondary phase. This corresponds to γ-Fe_2O_3, as demonstrated by the three peaks at 30.2°, 35.5° and 43.2° (JCPDS card n° 84–1595). Upon exposure to 650 °C for 1 h, the phase composition of the layer underwent a first evolution. The peaks related to the iron containing secondary phase totally disappeared, suggesting almost complete reduction of the iron oxide to elemental iron. In addition, the peaks of the fcc disordered phase became narrower and higher in intensity, implying significant alterations in the mean crystallite size. Despite these effects, no formation of any ordered phase was observed.

The situation was found to be significantly different after a 2 h annealing at 750 °C. Indeed, the two peaks related to the fcc phase totally disappeared and two new sets of peaks appeared [50,51]. The first, connected to the presence of an ordered $L1_0$ FePt phase (JCPDS card n° 43–1359), corresponds to the peaks located at 23.8°, 32.8°, 40.9°, 47.1°, 48.6° and 53.4°. These reflections are produced by the (001), (110), (111), (200), (002) and (201) orientations, respectively. In particular, the presence of the two superlattice peaks, (001) and (110), is the most important evidence of $L1_0$ formation. The second set, connected to the presence of an ordered $L1_2$ $FePt_3$ phase (JCPDS card n° 29–0716), corresponds to the peaks located at 23.0°, 32.8°, 40.5°, 47.1 and 53.4°. These reflections, which partially superimpose with the peaks of the $L1_0$ phase, are produced by the (100), (110), (111), (200) and (210) orientations, respectively. The XRD results obtained suggest the idea that the FePt sample annealed at 750 °C for 2 h is constituted by a mixture of ordered $L1_0$ FePt and $L1_2$ $FePt_3$ phases.

Fig. 5b shows the phase composition of the three different materials annealed at 750 °C for 2 h. Similarly to the equimolar, also the two remaining samples were constituted by a mixture of two among the phases appearing in the Fe—Pt phase diagram, i.e., $L1_0$ FePt and $L1_2$ $FePt_3$ phases [41]. However, the relative weight of the two phases changed according to the composition of the layer. Indeed, the content of $L1_0$ FePt increased moving from the Pt-rich sample to the equimolar and then to the Pt-poor sample. The Pt-poor sample was found to be almost phase pure, with only negligible amounts of $L1_2$ phase. Interestingly, the equimolar did not contain only $L1_0$ FePt, as the stoichiometry of the system would suggest, but also some $L1_2$ $FePt_3$. A similar phenomenon was observed also by Liu et al. [50], who synthesized FePt NPs using $Fe(NO_3)_3 \cdot 9H_2O$, $H_2PtCl_6 \cdot 6H_2O$ and $C_6H_8O_7 \cdot H_2O$. They observed that phase pure $L1_0$ NPs were obtained only in non-stoichiometric conditions (with an iron content around 60 % at.). A possible explanation can be the post-reduction of the surface segregated iron oxide to iron operated under the reducing H_2 atmosphere. This process may possibly make temporarily unavailable some of the iron at

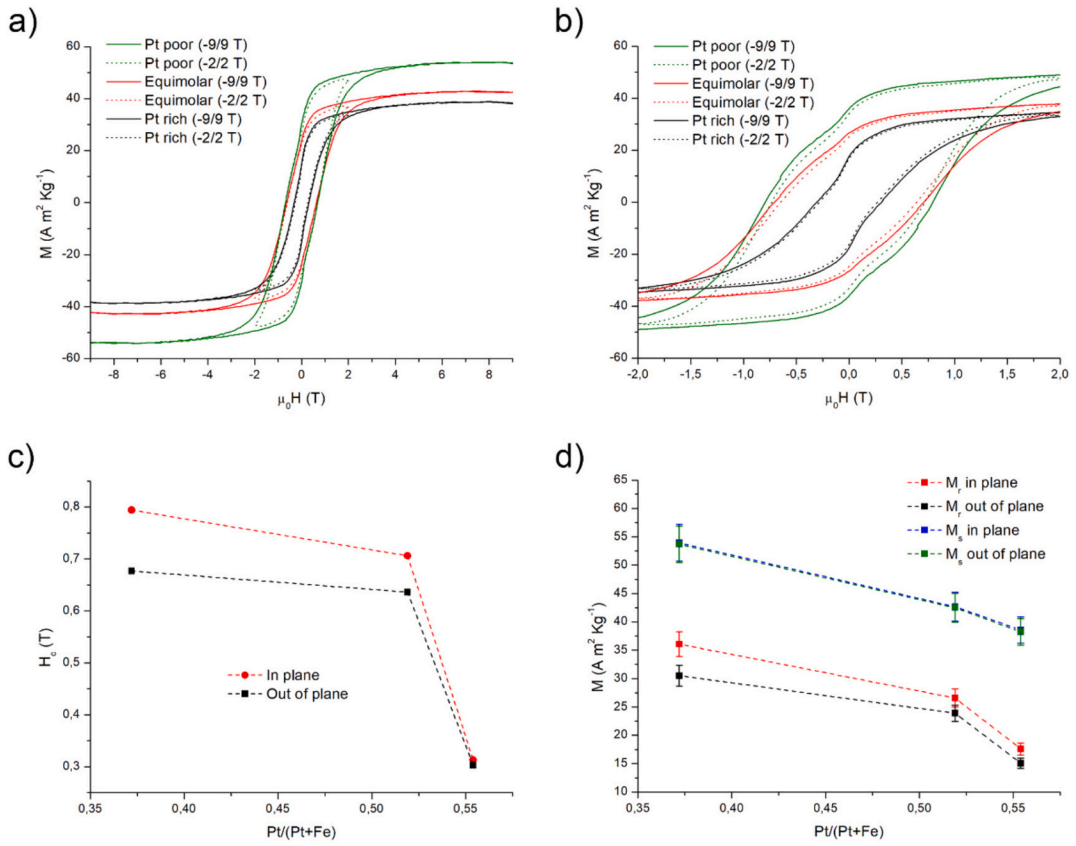

Fig. 7. (a) comparison between VSM (solid lines) and AGFM (dotted lines) out of plane results for alloys annealed at 750 °C as a function of their composition; (b) comparison between VSM (solid lines) and AGFM (dotted lines) in plane results for alloys annealed at 750 °C as a function of their composition; (c) alloy coercivity as a function of composition; (d) alloy remanence and saturation magnetization as a function of composition.

the beginning of the $L1_0$ phase formation. As a consequence, the material that contains from the beginning an excess of iron in the disordered fcc phase is probably favored for what concerns $L1_0$ phase formation.

Liu et al. also observed a strong displacement of the (111) peak connected to the presence of the $L1_0$ phase with respect to the composition of the alloy [50]. The same effect is visible for the NPs described in the present work in Fig. 5c, which represents a magnification of the (111) peak for the two phases $L1_0$ and $L1_2$. This effect is indicative of a progressive variation in the composition of the $L1_0$ phase, with a resulting alteration of its lattice parameters. As a consequence, the d-spacing was found to linearly vary with the FePt composition (Fig. 5d).

Finally, the mean crystallite dimension *s* was evaluated by measuring the FWHM (full width at half maximum) of the (111) peak and by using the value obtained in the Scherrer's law (eq. 2).

$$s = \frac{k\,\lambda}{\beta\cos\theta} \tag{2}$$

k is the dimensionless shape factor, λ is the wavelength of the X-rays employed, β represents the real line broadening (as the difference between the FWHM and the instrumental line broadening) and θ is the angle of the peak. Considering the results obtained in Fig. 5d, it is evident an interesting parallelism between the dimension of the NPs evaluated via TEM and the data extrapolated using the eq. 2. Indeed, the FePt NPs characterized by low mean diameters (Fig. 1g) yielded layers characterized by low mean crystallite size, and vice versa.

3.6. Magnetic properties characterization

As a first test of the magnetic response of the samples, hysteresis curves were measured by AGFM at room temperature up to a maximum field of 2 T. The results obtained in the in-plane and out-of-plane directions for the single samples are reported in Figures from S12 to S16, while the direct comparison between the samples is represented in Fig. 6. The reported magnetization values were evaluated starting from the measured magnetic moment by considering the layer thickness measured by SEM. A clear variation of the magnetic properties after annealing can be appreciated, with the as-printed layers showing a soft magnetic character and the layers annealed at 750 °C displaying hard magnetic properties.

The coercive field value measured for the as-printed layer (Fig. 6a and b) was of 10 mT, coherently with the presence of the chemically disordered and magnetically soft A1 phase. The curves measured by applying the magnetic field along different in-plane directions, and along the out-of-plane direction, showed no evident preferential magnetization orientation, due to the polycrystalline nature of the samples (Fig. 6a and b). The saturation magnetization value was of 20 A m^2 kg^{-1}, a significantly lower value compared to the bulk A1 phase of stoichiometric FePt, i.e. 80 A m^2 kg^{-1} [52]. Such a low magnetization value has to be ascribed, at least partially, to the oxidation evidenced by the compositional analysis and could additionally reflect the unavoidable overestimation of the effective density of the printed material.

Slight increases in coercive field and magnetization could be noticed after annealing at 650 °C, but the change was dramatic only after annealing the equimolar FePt layer at 750 °C (Fig. 6a and b). After annealing at the highest temperature, both magnetization and coercive field (H_c) values indeed clearly increased. The increase in magnetization followed the reduction in the amount of oxygen taking place after annealing. Anyhow, the magnetization values measured at 2 T on the annealed samples were lower than the bulk value for $L1_0$-FePt (35 vs. 76 A m^2 kg^{-1}). This could depend on the presence of a secondary phase (see below), but also partially reflect the error on the estimated magnetic volume and the fact that the maximum applied field was not sufficient to

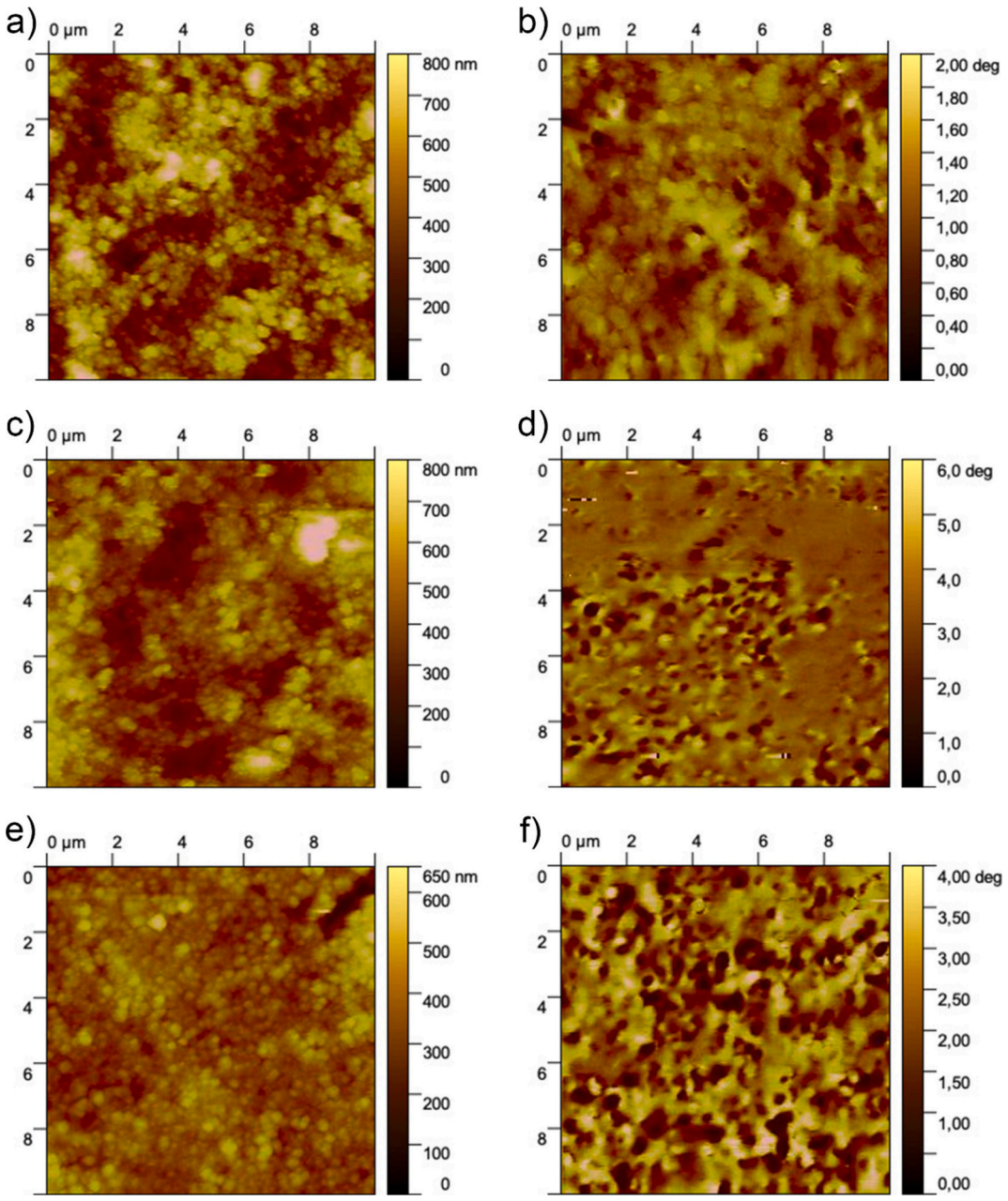

Fig. 8. (a) AFM and (b) MFM characterization of a Pt-rich FePt layer; (c) AFM and (d) MFM characterization of an equimolar FePt layer; (e) AFM and (f) MFM characterization of a Pt-poor FePt layer.

saturate the sample, due to the high anisotropy of the $L1_0$ phase. After the formation of the chemically ordered $L1_0$ phase, the magneto-crystalline anisotropy of the layer increased and gave rise to high coercive field values both in the in-plane and out-of-plane hysteresis curves. As a result, the coercive field values obtained after annealing were high for all the compositions, as evidenced in Figs. 5c and 5d.

Considering the lack of saturation observed with a maximum applied field of 2 T, additional magnetic characterization was carried out employing a VSM setup able to apply up to 9 T. Figs. 7a and 7b report the results obtained from the samples annealed at 750 °C, superimposed with the AGFM results for comparison. Figures from S17 to S19 show the direct comparison between the in-plane direction and the perpendicular one for the different samples. Saturation was effectively reached in all cases, and the measured hysteresis loops were all major. The general behavior of the material observed with the AGFM, as expected, was confirmed. The values of H_c and M_r, on the other hand, were found to be higher by a percentage ranging from 6 and 14 % (according to the composition of the alloy).

The trends of H_c, M_r and M_s values as a function of composition, reported in Figs. 7c and 7d, are in good agreement with the results of the XRD analysis. The coercive field decrease as a function of Pt content reflects the corresponding decrease in the content of $L1_0$ phase; the highest H_c value, i.e., 794 mT, was obtained for the Pt-poor layer, which shows the highest content in $L1_0$ phase. The occurrence of large coercive field values in both the in-plane and perpendicular hysteresis curves is a consequence of the polycrystalline nature of the samples. The Pt-poor sample also showed the highest measured value of M_s, i.e., 54 A m^2 kg^{-1}. Magnetization then decreased with increasing the Pt-content down to 38 A m^2 kg^{-1}, possibly due to the presence of the $FePt_3$ phase, which is characterized by lower magnetization, although as a secondary phase [52]. The shape of the hysteresis curves, that is, the presence of a double kink in the reversal process, indicates that in the

three samples also a magnetically softer phase is present, and this is the minority phase in the equimolar and Pt-poor samples. This softer magnetic behavior could be ascribed either to a residual A1 phase or to the $FePt_3$ phase.

The significant values of coercive field and magnetization measured on the inkjet printed layers indicate these materials as promising candidates for microscale permanent magnets. As further confirmation of the good magnetic properties, the annealed layers in the thermally-demagnetized state were studied by AFM and MFM. The results are reported in Fig. 8. AFM evidences a granular morphology with surface roughness up to 150 nm, coherently with SEM. The roughness changes from area to area. Specific values of the Root Mean Square Roughness (R_q) for the topography images in the left panels of Fig. 8 are 145.50 nm for the Pt-rich layer, 123.00 nm for the equimolar layer and 130.8 nm for the Pt-poor layer. The MFM images in the right panels display a spatially irregular contrast, due to a significant out-of-plane stray field. This contrast originates from the presence of high anisotropy grains with a perpendicular component of the easy magnetization axis. However, the comparison between AFM and MFM images taken on the same sample and same area (i.e., a-b, c-d, e-f) shows that the microstructures appearing as bright/dark contrast areas are much larger than the grain size, and can thus be associated to inter-grain magnetic domains with irregular shape and size. In order to clarify this point, some of these typical bright/dark areas appearing in Fig. 8b are highlighted by blue circles in Fig. S20. A careful analysis of the three samples in different areas and scanning different spatial scales (from 1 μm to 50 μm), revealed that the Pt-rich sample shows a larger fraction of the surface with no MFM contrast. This is coherent with what concluded after the magnetometry characterization, about the higher fraction of magnetically soft phase in the Pt-rich sample compared to the equimolar and Pt-poor samples. In some of the scans, only a few areas of this type are visible, such as in Fig. 8b. The lower magnetic anisotropy of the soft phase indeed favors the in-plane orientation of magnetic moments, due to the predominance of shape anisotropy.

A step forward for realizing high performance permanent magnets using this printing method would be obtaining oriented layers and further reducing the minor softer magnetic phase, which represents a disadvantage for specific applications requiring high values of squareness, such as in magnetic circuits where the magnet works under strong demagnetizing conditions.

4. Conclusions

This work demonstrates, for the first time, the use of inkjet printing as a methodology to fabricate hard magnetic FePt thin layers. The developed process successfully employed FePt nanoparticles dispersed in a green solvent to obtain stable, printable inks. The deposited layers, after undergoing high temperature annealing in a reducing atmosphere, exhibited the characteristic hard magnetic $L1_0$ phase, as confirmed by XRD analysis. The printed FePt layers showed substantial magnetic hardness, with the highest observed coercivity value at 794 mT and the highest remanence at 36 A m^2 kg^{-1}. These magnetic properties are highly attractive for many applications, making the FePt thin layers obtained potentially suitable for the fabrication of microactuators, energy harvesters and magnetic sensors. Additionally, the ability to control the shape of the printed area through inkjet deposition provides a pathway for future advancements in patterned magnetic structures. In general, the findings of the present work open new possibilities for the scalable and cost-effective manufacturing of high-performance FePt-based magnetic components.

CRediT authorship contribution statement

Roberto Bernasconi: Writing – review & editing, Writing – original draft, Visualization, Validation, Methodology, Investigation, Formal analysis, Data curation, Conceptualization. **Francesca Casoli:** Writing – review & editing, Writing – original draft, Visualization, Validation, Resources, Methodology, Investigation, Data curation. **Luca Magagnin:** Supervision, Resources, Project administration, Methodology.

Declaration of competing interest

The authors declare that they have no known competing financial interests or personal relationships that could have influenced the work described in the present paper.

Appendix A. Supplementary data

Supplementary data to this article can be found online at https://doi.org/10.1016/j.mseb.2025.119160.

Data availability

Data will be made available on request.

References

[1] P. Vlaic, E. Burzo, Magnetic behaviour of iron-platinum alloys, J. Optoelectron. Adv. Mater. 12 (2010) 1114.

[2] D.E. Laughlin, K. Srinivasan, M. Tanase, L. Wang, Crystallographic aspects of L10 magnetic materials, Scr. Mater. 53 (2005) 383–388, https://doi.org/10.1016/j.scriptamat.2005.04.039.

[3] J.C. Lodder, L.T. Nguyen, FePt thin films: fundamentals and applications, in: Encycl. Mater. Sci. Technol, Elsevier, 2005, pp. 1–10.

[4] P. Tozman, S. Isogami, I. Suzuki, A. Bolyachkin, H. Sepehri-Amin, S.J. Greaves, H. Suto, Y. Sasaki, T.Y. Chang, Y. Kubota, P. Steiner, P.W. Huang, K. Hono, Y. K. Takahashi, Dual-layer FePt-C granular media for multi-level heat-assisted magnetic recording, Acta Mater. 271 (2024) 119869, https://doi.org/10.1016/j.actamat.2024.119869.

[5] M. Toda, H. Xu, T. Ono, Electroplated FePt films for micromechanical magnetic sensors, Phys. Status Solidi Appl. Mater. Sci. 218 (2021) 6–11, https://doi.org/10.1002/pssa.202000547.

[6] J.M.D. Coey, Hard magnetic materials: a perspective, IEEE Trans. Magn. 47 (2011) 4671–4681, https://doi.org/10.1109/TMAG.2011.2166975.

[7] J. Giltinan, V. Sridhar, U. Bozuyuk, D. Sheehan, M. Sitti, 3D microprinting of Iron platinum nanoparticle-based magnetic Mobile microrobots, Adv. Intell. Syst. 3 (2021) 2000204, https://doi.org/10.1002/aisy.202000204.

[8] V.M. Kadiri, J.-P. Günther, S.N. Kottapalli, R. Goyal, F. Peter, M. Alarcón-Correa, K. Son, H.-N. Barad, M. Börsch, P. Fischer, Light-and magnetically actuated FePt microswimmers, Eur. Phys. J. E: Soft Matter Biol. Phys. 44 (2021) 1–11.

[9] T. Shima, K. Takanashi, G.Q. Li, S. Ishio, Microstructure and magnetic properties for highly coercive FePt sputtered films, Mater. Trans. 44 (2003) 1508–1513, https://doi.org/10.2320/matertrans.44.1508.

[10] K. Hono, Y.K. Takahashi, G. Varvaro, F. Casoli, in: G. Varvaro, F. Casoli (Eds.), L10 FePt Granular Films for Heat-Assisted Magnetic Recording Media, Ultrah, Density Magn. Rec, 2016, pp. 246–277.

[11] C. Qi, Y. Miyahara, Z. Wang, N. Sugita, M. Nakano, T. Shinshi, An electromagnetic microactuator with tunable dynamic characteristics using a thick-film FePt permanent magnet, AIP Adv. 14 (2024).

[12] Y. Ying, H. Wang, J. Zheng, J. Yu, W. Li, L. Qiao, W. Cai, S. Che, Preparation, microstructure, and magnetic properties of electrodeposited Nanocrystalline L10 FePt films, J. Supercond. Nov. Magn. 33 (2020) 3563–3570, https://doi.org/10.1007/s10948-020-05624-w.

[13] R. Bernasconi, A. Nova, S. Pané, L. Magagnin, Electrodeposition of Equiatomic FePt permanent magnets from non-aqueous electrolytes based on ethylene glycol, J. Electrochem. Soc. 169 (2022) 072506, https://doi.org/10.1149/1945-7111/ac81f8.

[14] F.M.F. Rhen, J.M.D. Coey, Electrodeposition of coercive L10 FePt magnets, J. Magn. Magn. Mater. 322 (2010) 1572–1575.

[15] R. Magalhães, M.P. Proenca, J.P. Araújo, C. Nunes, A.M. Pereira, C.T. Sousa, Fabrication of FePt nanowires through pulsed electrodeposition into nanoporous alumina templates, Appl. Nanosci. 12 (2022) 3573–3584, https://doi.org/10.1007/s13204-022-02454-1.

[16] K.J. Merazzo, A.C. Lima, M. Rincón-Iglesias, L.C. Fernandes, N. Pereira, S. Lanceros-Mendez, P. Martins, Magnetic materials: a journey from finding north to an exciting printed future, Mater. Horiz. 8 (2021) 2654–2684, https://doi.org/10.1039/d1mh00641j.

[17] H.-E.-J. Moni, B. Rezaei, I.H. Karampelas, M. Saeidi-Javash, J. Gómez-Pastora, K. Wu, M. Zeng, Printing rare-earth-free (REF) magnetic inks: synthesis, formulation, and device applications, Nanoscale 17 (2025) 4830–4853.

[18] B. Rezaei, H.E.J. Moni, I.H. Karampelas, A. Sharma, S. Mostufa, E. Azizi, X. Liu, M. Zeng, J. Gómez-Pastora, R. He, K. Wu, Additive manufacturing of magnetic materials for energy, environment, healthcare, and industry applications, Adv. Funct. Mater. 2416823 (2024) 1–29, https://doi.org/10.1002/adfm.202416823.

[19] H. Song, J. Spencer, A. Jander, J. Nielsen, J. Stasiak, V. Kasperchik, P. Dhagat, Inkjet printing of magnetic materials with aligned anisotropy, J. Appl. Phys. 115 (2014) 3–6, https://doi.org/10.1063/1.4863168.
[20] K.N. Al-Milaji, R.L. Hadimani, S. Gupta, V.K. Pecharsky, H. Zhao, Inkjet printing of magnetic particles toward anisotropic magnetic properties, Sci. Rep. 9 (2019) 1–9, https://doi.org/10.1038/s41598-019-52699-0.
[21] S.D. Hoath, Fundamentals of Inkjet Printing: The Science of Inkjet and Droplets, John Wiley & Sons, 2016.
[22] M. Bissannagari, J. Kim, Inkjet printing of NiZn-ferrite films and their magnetic properties, Ceram. Int. 41 (2015) 8023–8027.
[23] M. Cannamela, J. Stasiak, P. Harmon, T. Allen, P. Dhagat, Fabrication of Magnetic Polymer Nanocomposites Using Inkjet 3D Print Technology, in: NIP Digit. Fabr. Conf., Society for Imaging Science and Technology, 2020, pp. 1–5.
[24] D. Hrakova, P. Ripka, A. Laposa, D. Novotny, J. Kroutil, V. Povolný, O. Kaman, P. Veverka, Inkjet-printed Mn-Zn ferrite nanoparticle core for fluxgate, J. Magn. Magn. Mater. 563 (2022) 170003.
[25] L. Wu, J. Li, C. Liu, R. Zheng, J. Li, X. Wang, M. Li, J. Wei, Inkjet printed BiFeO3 thin films with non-volatile resistive switching behaviors, Phys. Lett. A 404 (2021) 127406.
[26] M. Mariani, F. Cervellera, E. Migliori, F. Maspero, R. Bernasconi, C. Galassi, L. Magagnin, N. Lecis, Inkjet printing of cobalt ferrite for hard ferromagnetic thick films manufacturing, Adv. Eng. Mater. 26 (2024) 1–13, https://doi.org/10.1002/adem.202400371.
[27] L. Suber, G. Marchegiani, E.S. Olivetti, F. Celegato, M. Coïsson, P. Tiberto, P. Allia, G. Barrera, L. Pilloni, L. Barba, F. Padella, P. Cossari, A. Chiolerio, Pure magnetic hard fct FePt nanoparticles: chemical synthesis, structural and magnetic properties correlations, Mater. Chem. Phys. 144 (2014) 186–193, https://doi.org/10.1016/j.matchemphys.2013.12.041.
[28] M. Chen, J.P. Liu, S. Sun, One-step synthesis of FePt nanoparticles with tunable size, J. Am. Chem. Soc. 126 (2004) 8394–8395, https://doi.org/10.1021/ja047648m.
[29] S. Sun, Recent advances in chemical synthesis, self-assembly, and applications of FePt nanoparticles, Adv. Mater. 18 (2006) 393–403, https://doi.org/10.1002/adma.200501464.
[30] X.J. Bai, Y.Y. Zhang, L. Chen, C.D. Cao, W.X. Zhang, W.L. Zhang, Low-temperature ordering of FePt nanoparticles by alternate reduction of metal salts in aqueous medium, J. Magn. Magn. Mater. 349 (2014) 284–287, https://doi.org/10.1016/j.jmmm.2013.09.014.
[31] J.P. Wang, J.M. Qiu, T.A. Taton, B.S. Kim, Direct preparation of highly ordered L10Phase FePt nanoparticles and their shape-assisted assembly, IEEE Trans. Magn. 42 (2006) 3042–3047, https://doi.org/10.1109/TMAG.2006.880150.
[32] V. Velasco, A. Hernando, P. Crespo, FePt magnetic particles prepared by surfactant-assisted ball milling, J. Magn. Magn. Mater. 343 (2013) 228–233, https://doi.org/10.1016/j.jmmm.2013.05.017.
[33] F.Y. Acquaye, R. Mahat, S. Street, Synthesis of FePt nanoparticles by Photoreduction and chemical reduction in poly(ethyleneimine), Langmuir 37 (2021) 11750–11758, https://doi.org/10.1021/acs.langmuir.1c01662.
[34] J. Yang, Y. Jiang, Y. Liu, X. Zhang, Y. Wang, Y. Zhang, J. Wang, W. Li, X. Cheng, Effects of SiO2 content on the structure and magnetic properties of L10-FePt nanoparticles synthesized by the sol-gel method, Mater. Lett. 91 (2013) 348–351, https://doi.org/10.1016/j.matlet.2012.08.125.
[35] S. Liang, Q. Zhou, M. Wang, Y. Zhu, Q. Wu, X. Yang, Water-soluble L-cysteine-coated FePt nanoparticles as dual MRI/CT imaging contrast agent for glioma, Int. J. Nanomedicine 2325–2333 (2015).
[36] X. Liu, H. Wang, S. Zuo, T. Zhang, Y. Dong, D. Li, C. Jiang, Dispersible and manipulable magnetic L10-FePt nanoparticles, Nanoscale 12 (2020) 7843–7848, https://doi.org/10.1039/c9nr10302c.
[37] K. Sato, B. Jeyadevan, K. Tohji, Preparation and properties of ferromagnetic FePt dispersion, J. Magn. Magn. Mater. 289 (2005) 1–4, https://doi.org/10.1016/j.jmmm.2004.11.002.
[38] E. Hernández-Pagán, A. Yazdanshenas, D.J. Boski, J. Bi, H.R. Lacey, O.J.M. Piza, C. C.S. Sierra, Cyrene as solvent for metal nanoparticle synthesis, J. Nanopart. Res. 26 (2024) 200.
[39] R. Poon, I. Zhitomirsky, Application of Cyrene as a solvent and dispersing agent for fabrication of Mn3O4-carbon nanotube supercapacitor electrodes, Colloid Interface Sci. Commun. 34 (2020) 100226.
[40] R.N. Patel, A.T. Heitsch, C. Hyun, D.-M. Smilgies, A. De Lozanne, Y.-L. Loo, B. A. Korgel, Printed magnetic FePt nanocrystal films, ACS Appl. Mater. Interfaces 1 (2009) 1339–1346.
[41] H. Okamoto, Fe-Pt (Iron-platinum), J. Phase Equilib. Diffus. 25 (2004) 395, https://doi.org/10.1361/15477030420241.
[42] N. Xiaomin, S. Xiaobo, Z. Huagui, Z. Dongen, Y. Dandan, Z. Qingbiao, Studies on the one-step preparation of iron nanoparticles in solution, J. Cryst. Growth 275 (2005) 548–553, https://doi.org/10.1016/j.jcrysgro.2004.12.009.
[43] B. Derby, Inkjet printing of functional and structural materials: fluid property requirements, feature stability, and resolution, Annu. Rev. Mater. Res. 40 (2010) 395–414.
[44] B. Derby, Inkjet printing ceramics: from drops to solid, J. Eur. Ceram. Soc. 31 (2011) 2543–2550.
[45] P. He, B. Derby, Controlling coffee ring formation during drying of inkjet printed 2D inks, Adv. Mater. Interfaces 4 (2017) 2–7, https://doi.org/10.1002/admi.201700944.
[46] F. Langer, S. Yin, J. Duvigneau, G.J. Vancso, N. Benson, Suppression of the coffee ring effect in a single solvent-based silicon nanoparticle ink, ACS Appl. Mater. Interfaces 16 (2024) 4242–4248.
[47] G.R. Chandel, J. Sun, S.A. Etha, B. Zhao, V.S. Sivasankar, S. Nikfarjam, M. Wang, D. R. Hines, A. Dasgupta, T. Woehl, S. Das, Direct visualization of nanoparticle morphology in thermally sintered nanoparticle ink traces and the relationship among nanoparticle morphology, incomplete polymer removal, and trace conductivity, Nanotechnology 34 (2023), https://doi.org/10.1088/1361-6528/acd9d2.
[48] J. Yuan, P. Wu, X. Hu, J. Qian, Oxidation induced alloy composition and magnetic property change in FePt thin film, in: 2005 IEEE Int. Magn. Conf, IEEE, 2005, pp. 881–882.
[49] J. Yu, D. Han, Y. Ying, L. Qiao, J. Zheng, W. Li, J. Li, W. Cai, S. Che, N. Wakiya, H. Suzuki, Influence of particle size on the spin pinning effect in the fcc-FePt nanoparticles, J. Supercond. Nov. Magn. 32 (2019) 1501–1505, https://doi.org/10.1007/s10948-019-5091-7.
[50] Y. Liu, Y. Jiang, X. Zhang, Y. Wang, Y. Zhang, H. Liu, H. Zhai, Y. Liu, J. Yang, Y. Yan, Structural and magnetic properties of the ordered FePt3, FePt and Fe3Pt nanoparticles, J. Solid State Chem. 209 (2014) 69–73, https://doi.org/10.1016/j.jssc.2013.10.027.
[51] J. Yu, W. Gao, F. Liu, Y. Ju, F. Zhao, Z. Yang, X. Chu, S. Che, Y. Hou, Tuning crystal structure and magnetic property of dispersible FePt intermetallic nanoparticles, Sci. China-Mater. 61 (2018) 961–968, https://doi.org/10.1007/s40843-017-9203-9.
[52] J. Lyubina, I. Opahle, K.-H. Müller, O. Gutfleisch, M. Richter, M. Wolf, L. Schultz, Magnetocrystalline anisotropy inL10 FePt and exchangecoupling in FePt/Fe3Pt nanocomposites, J. Phys. Condens. Matter 17 (2005) 4157.